Trajectory of a Liquid Jet Traversing Subsonic Airstreams

Takao Inamura*
Hirosaki University, Hirosaki 036, Japan

Introduction

FUEL-JET penetration is especially important in regards to combustor design and in understanding the physics of liquid-jet disintegration. Thomas and Schetz[1] researched about the spray characteristics of a liquid jet traversing supersonic airstreams. They studied liquid-jet penetrations, mean droplet diameter profiles, and droplet mass-flux profiles. Inamura and coworkers[2,3] and Oda et al.[4] studied jet penetration, jet width, and the spray characteristics in subsonic airstreams. Tsau et al.[5] numerically analyzed the behavior of a liquid jet that had been transversely injected into subsonic airstreams. Wu et al.[6] deduced the semi-empirical equation of liquid-jet penetration traversing subsonic airstreams. They estimated the drag coefficients of a liquid jet by using jet-penetration measurements.

There has been a great deal of research on the trajectories of liquid-jet traversing supersonic airstreams. However, there has been little done on the theoretical analysis of the trajectory of a liquid jet traversing subsonic airstreams. The objective of this paper is to semitheoretically deduce a simplified equation for the trajectory of a liquid jet traversing subsonic airstreams, which is useful for the easy design of a combustor.

Theoretical Analysis

The penetration of fuel with normal injection into an airstream can be divided into two stages. The first is the penetration of the liquid jet before its disintegration, and the second one is that of the spray plume after liquid-jet disintegration. This paper is limited to the trajectory of a liquid jet before its disintegration because this topic is very important in regards to understanding the disintegration process and characterizing the resulting atomization.

This analysis of liquid-jet deformation is based on Clark's model.[7,8] The assumption is made that the cross section of a liquid jet is deformed from a circular shape at the nozzle exit to an ellipsoidal shape by the dynamic airstream pressure. The sectional area of a liquid jet is constant along its trajectory. The assumption is also made that the effects of the disturbance wave on the liquid-jet surface on the trajectory are negligible.

Figure 1 shows the geometry of the cross section of a liquid jet. The motion of the center of mass of the half-liquid jet with unit thickness along the jet axis can be expressed by the following equation:

$$\frac{1}{2}\pi r_0^2 \rho_j \frac{\mathrm{d}^2 w}{\mathrm{d}t^2} = F_v + F_s + F_p \tag{1}$$

where r_0, ρ_j, and w indicate the radius of the initial liquid jet at the nozzle exit, the density of a liquid jet, and the distance from the center axis of a liquid jet to the center of mass of the half-liquid jet, which has an ellipsoidal cross section with major semiaxis a and minor semiaxis b and unit thickness along the jet axis, respectively. F_v, F_s, and F_p indicate the viscous force, the surface tension force, and the external force because of the airstream, respectively.

If we substitute $w = w_0 + r_0 w'$ where w_0 is the w of the undeformed initial liquid jet, Eq. (1) becomes

$$\frac{1}{2}\pi r_0^3 \rho_j \frac{\mathrm{d}^2 w'}{\mathrm{d}t^2} = F_v + F_s + F_p \tag{2}$$

Received 29 May 1997; revision received 3 August 1999; accepted for publication 9 August 1999.

*Professor, Faculty of Science and Technology. Member AIAA.

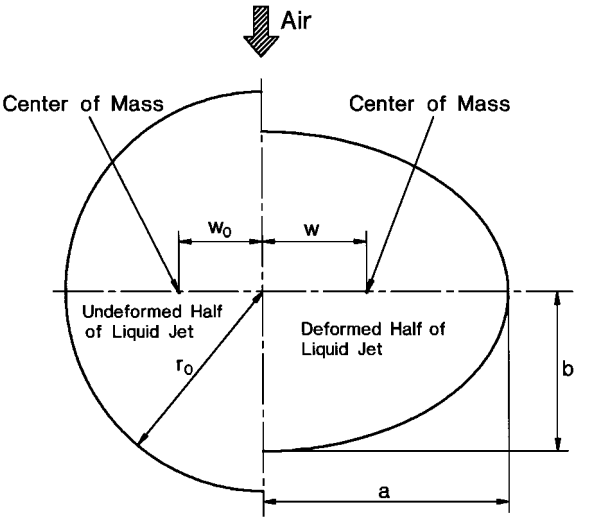

Fig. 1 Geometry of cross section of liquid jet.

The viscous force can be expressed by the following equation[7]:

$$F_v = -\frac{9}{8}\pi^3 \mu_j r_0 \frac{\mathrm{d}w'}{\mathrm{d}t} \tag{3}$$

where μ_j indicates the viscosity of the liquid jet. The surface tension force can be expressed by the following equation[7]:

$$F_s = -\tfrac{9}{8}\pi^3 \sigma w' \tag{4}$$

where σ indicates the surface tension of the liquid jet. Assuming that the deformation of the liquid jet is small, the external force because of the airstream can be estimated as follows[7]:

$$F_p = r_0 \rho_a v_r^2 \approx r_0 \rho_a v_a^2 \tag{5}$$

where ρ_a and v_r indicate the density of the air and the relative velocity, respectively, between the airstream and the liquid jet, the value approximately equals the air velocity v_a.

Substituting Eqs. (3), (4), and (5) into Eq. (2) and dropping the primes of w, the differential equation for the center of mass of the half-liquid jet with unit thickness can be obtained as follows:

$$\frac{\pi}{2} r_0^3 \rho_j \frac{\mathrm{d}^2 w}{\mathrm{d}t^2} + \frac{9}{8}\pi^3 \mu_j r_0 \frac{\mathrm{d}w}{\mathrm{d}t} + \frac{9}{8}\pi^3 \sigma w = r_0 \rho_a v_a^2 \tag{6}$$

Next, taking the equilibrium of a liquid jet with unit thickness in the airstream direction into account gives the following equation:

$$\pi r_0^2 \rho_j \frac{\mathrm{d}^2 x}{\mathrm{d}t^2} = c_D \frac{1}{2} \rho_a v_a^2 2a \tag{7}$$

where x and c_D indicate the coordinate in the direction of the airstream and the drag coefficient of the liquid jet, respectively. The assumption that the deformation of the liquid jet is small gives the following equation:

$$c_D \approx 1.0 \tag{8}$$

Substituting Eq. (8) into Eq. (7) gives the following equation:

$$\frac{\mathrm{d}^2 x}{\mathrm{d}t^2} = \frac{a}{\pi r_0^2} \frac{\rho_a}{\rho_j} v_a^2 \tag{9}$$

The assumption that the sectional area of a liquid jet is constant along its trajectory gives the following equations:

$$ab = r_0^2 \tag{10}$$

$$\left(\frac{\mathrm{d}x}{\mathrm{d}t}\right)^2 + \left(\frac{\mathrm{d}y}{\mathrm{d}t}\right)^2 = v_j^2 \tag{11}$$

where y is the coordinate in the direction of the liquid injection, which is perpendicular to that of the airstream, and v_j indicates the injection velocity of the liquid jet.

Because w and w_0 indicate the distance from the center axis to the center of mass of the half-liquid jet, which has an ellipsoidal cross section with major semiaxis a and minor semiaxis b and unit thickness, and that of a half cylinder, which has a circular cross section with radius r_0 and unit thickness, respectively, the following equations can be obtained:

$$w = 4a/3\pi \tag{12}$$

$$w_0 = 4r_0/3\pi \tag{13}$$

Because Eqs. (9) and (11) give the trajectory of the liquid jet axis, the following coordinate transformations are needed to obtain liquid-jet penetration:

$$X = x + r_0 - b = x + r_0 - r_0^2/a \tag{14}$$

$$Y = y \tag{15}$$

where X and Y are the coordinates of the liquid-jet penetration. The origin of this coordinate system is set on the upstream side of the liquid nozzle exit.

Results and Discussion

Equations (6), (9), (11), and (12) were solved numerically and simultaneously by using the Runge–Kutta method. The liquid-jet penetrations were obtained by using the coordinate transformations from Eqs. (14) and (15).

The penetration depths of the liquid jet traversing subsonic airstreams, however, were experimentally measured. The experimental apparatus and airflow structure near the liquid nozzle exit are described in detail in a previous paper.[3] Variations in the mean air velocity in the cross section of the wind tunnel are less than 4% of the maximum mean velocity. Boundary-layer thickness is estimated to be around 2 mm at the exit of the liquid nozzle. The penetrations were measured by using two backlighted instantaneous photographs that had been magnified 10 times. Where the surface of the liquid jet was wavy, the midpoint between the crest and the trough of the surface wave was measured as the penetration. The uncertainty in penetration measurements was estimated to be less than 20 μm. The repeatability of the liquid-jet injection is relatively reliable as shown in Figs. 2.

Figures 2 shows the comparisons of the liquid-jet penetration between the measurements, the present calculations, and the proposed empirical equations.[2,6] The liquid jets whose penetrations are compared with calculations in the figures mean liquid column according to the cited references. The value q in this figure indicates the liquid-to-air momentum ratio, which equals $\rho_j v_j^2/\rho_a v_a^2$. At $V_a = 53.0$ m/s these calculations were almost the same as the measurements. Under low air velocity condition ($V_a = 30.0$ m/s) the preceding calculations overestimated the penetrations for the whole range of $X/(2r_0)$. Under high air velocity condition ($V_a = 75.0$ m/s), however, the calculations underestimated them. These discrepancies appear to be caused by the estimation of the drag coefficient. In this paper the drag coefficient of the liquid jet was assumed to be constant as is shown in Eq. (8). However, the drag coefficient of a cylinder is a function of the Reynolds number. From the comparisons between the calculations and the measurements, the drag coefficient was estimated to be larger than 1.0 under low air velocity conditions and smaller than 1.0 under high air velocity conditions.

The empirical equations showed larger penetrations than the calculations and the measurements in this paper, which seems to be because of the difference in airflow structure near the liquid nozzle exit. In addition, the proposed equations covered the whole area by only one equation, and the penetration in the vicinity of the nozzle exit appeared to be not very important in regards to combustor design. This implies that the discrepancies between the empirical equation, and the measurement become larger in the vicinity of the nozzle exit.

Because the present calculation includes several assumptions, the application is limited to the case where no large deformation of a liquid jet takes place, and no droplet is shed from the jet surface in the region under consideration, that is, the low-speed airstream condition.

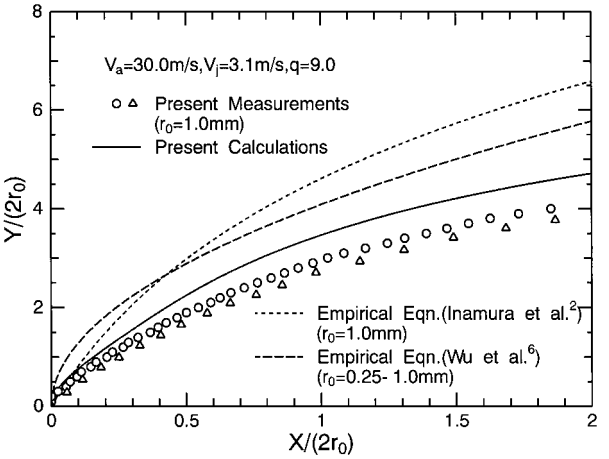

a) V_a = 30.0 m/s, V_j = 3.1 m/s

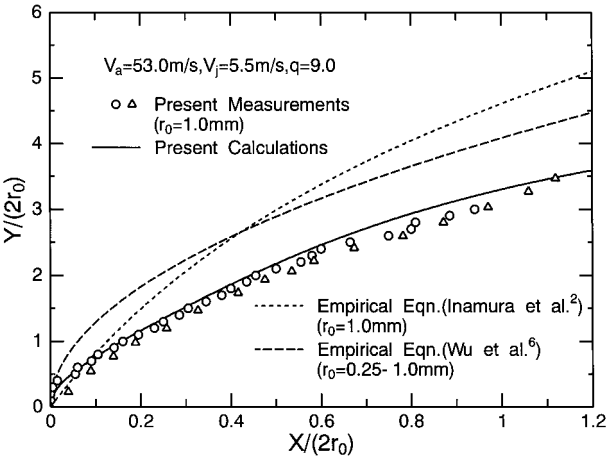

b) V_a = 53.0 m/s, V_j = 5.5 m/s

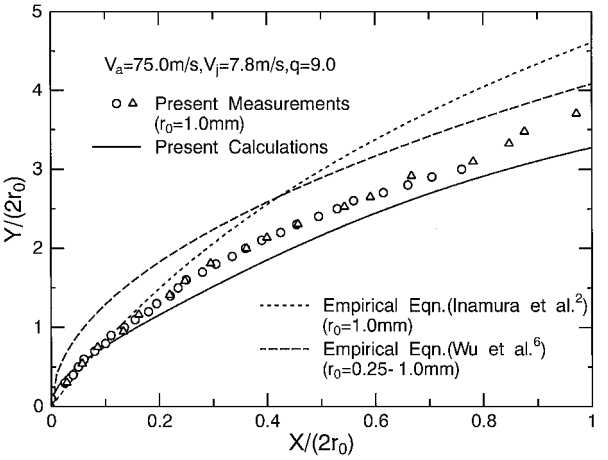

c) V_a = 75.0 m/s, V_j = 7.8 m/s

Fig. 2 Comparisons of liquid-jet penetration.

Conclusions

The penetration of a liquid jet traversing subsonic airstreams was semitheoretically obtained and compared with jet-penetration measurements. The calculated penetrations were almost the same as the measurements that were taken when the air velocity was equal to 53.0 m/s. The present calculations overestimated the penetrations in the case of smaller air velocity and underestimated them in the case of larger air velocity. Further research about the drag coefficients of liquid jets should be performed to predict more accurately their trajectories.

References

[1]Thomas, R. H., and Schetz, J. A., "Distributions Across the Plume of Transverse Liquid and Slurry Jets in Supersonic Airflow," *AIAA Journal*, Vol. 23, No. 12, 1985, pp. 1892–1901.

[2]Inamura, T., Nagai, N., Watanabe, T., and Yatsuyanagi, N., "Disintegration of Liquid and Slurry Jets Traversing Subsonic Airstreams," *Proceedings of the Third World Conference on Experimental Heat Transfer, Fluid Mechanics and Thermodynamics*, Elsevier, Amsterdam, 1993, pp. 1522–1529.

[3]Inamura, T., and Nagai, N., "Spray Characteristics of Liquid Jet Traversing Subsonic Airstreams," *Journal of Propulsion and Power*, Vol. 13, No. 2, 1997, pp. 250–256.

[4]Oda, T., Nishida, K., and Hiroyasu, H., "Characterization of Liquid Jet Atomization Across a High-Speed Airstream by Laser-Sheet Tomography," *Proceedings of the 6th International Conference on Liquid Atomization and Spray Systems*, Begell House, New York, 1994, pp. 624–631.

[5]Tsau, F., Elghobashi, S., and Sirignano, W. A., "Prediction of a Liquid Jet in a Gaseous Crossflow," AIAA Paper 90-2067, July 1990.

[6]Wu, P.-K., Kirkendall, K. A., Fuller, R. P., and Nejad, A. S., "Breakup Processes of Liquid Jets in Subsonic Crossflows," *Journal of Propulsion and Power*, Vol. 13, No. 1, 1997, pp. 64–73.

[7]Clark, M. M., "Drop Breakup in a Turbulent Flow—I. Conceptual and Modeling Considerations," *Chemical Engineering Science*, Vol. 43, No. 3, 1988, pp. 671–679.

[8]Ibrahim, E. A., Yang, H. Q., and Przekwas, A. J., "Modeling of Spray Droplets Deformation and Breakup," *Journal of Propulsion and Power*, Vol. 9, No. 4, 1993, pp. 651–654.

Preliminary Mass Spectrometry of a Xenon Hollow Cathode

Mark W. Crofton*

The Aerospace Corporation,
El Segundo, California 90245-4691

Nomenclature

E = kinetic energy
e = elementary unit of charge
I_{ck} = cathode keeper current
I_h = cathode heater current
m = particle mass
n = ion charge number
V_{ck} = cathode keeper voltage, referenced to the grounded cathode

Introduction

XENON hollow cathodes can produce single-point failures in a number of electric thrusters and are an important factor regarding erosion of the screen grid and other components in ion engines. During operation at the high-emission current required for high-power ion propulsion systems, the orifice and any components in the plume erode rapidly.[1] Ions of sufficient energy to cause significant erosion have been observed in plume experiments.[2–4]

Past measurements of the ion kinetic energy distribution in the far field have been performed with a retarding potential analyzer (RPA) or an energy analyzer.[2–4] The results revealed that a very broad energy distribution exists in the high-current regime. The data indicate that ions are abundantly formed with energies as much as several times higher than eV_{ck}. Unfortunately, RPA and energy analyzer devices do not distinguish between xenon ions having different charge states but the same value of E/ne.

The mechanism by which the high-energy ions arise is not established, but two principal hypotheses have been put forward. One theoretical explanation that has been offered invokes the formation of a potential hill a few millimeters downstream from the orifice.[3,5] Although consistent with the data, no clear understanding has emerged of the means by which a hill of sufficient height could be formed. An alternative mechanism has been postulated whereby the current density at the orifice (on the order of 10^4 A cm^{-2}) results in ion acceleration via a magnetohydrodynamic effect.[2] The possible presence of abundant multiply charged ions and their role in producing energetic singly charged species has not been considered in either case.

Spatially resolved experimental measurements of electric potential and the ion velocities near the hollow cathode orifice are needed to fully resolve the mechanistic issue. In the present study, a quadrupole mass spectrometer provided a simple means of monitoring ions according to m/ne and easily resolved the charge states of xenon. Under special circumstances, the same experimental setup was able to detect barium atoms in the plume. The technique is suitable for monitoring cathode effluents during conditioning, startup, and normal operation.

Experimental

The hollow cathode was installed in a 75-cm-diam vacuum chamber, pumped by a 1000 l/s (on nitrogen) turbomolecular pump and a 12,500/4,500/~1,000 l/s (hydrogen/water/xenon) TMP150 cryopump (CVI) mounted on a 10-in. Conflat® flange.[6] The cryopump could be readily isolated from the chamber by an 8-in. electropneumatic gate valve. The base pressure with no xenon flow was 6×10^{-8} torr. Under the fixed xenon flow rate of 0.105 mg/s, the background pressure indicated by an ion gauge positioned far from the cryopump was about 1.5×10^{-5} torr, after applying a standard sensitivity correction for xenon.

The T5 xenon hollow cathode was installed in a fixed orientation, with a quadrupole mass spectrometer (QMS) monitoring the plume centerline through a beam skimmer. The grounded skimmer with 5-mm aperture was mounted 17 cm downstream from the cathode orifice. The entrance of an SRS200 QMS for residual gas analysis was about 22 cm farther downstream, aligned with the hollow cathode orifice and beam skimmer. A simple modification of the QMS electronics allowed operation with the ionizer turned on or off.

The hollow cathode contained an impregnated tungsten dispenser, 1.0-mm i.d. $\times$2.8-mm o.d. $\times$11 mm, that acts as a chemical factory to release barium to the surface at an appropriate rate to achieve low work function and long life. The orifice, machined out of solid tantalum, was 0.2 mm in diameter $\times$1.0 mm long, with a downstream full-angle chamfer of 90 deg. A keeper electrode with 3-mm-diam aperture was positioned just downstream in an enclosed configuration. The hollow cathode had not been operated prior to this study.

Results and Discussion

The mass spectrum of Fig. 1 was obtained with the ionizing filament on. It shows the predominance of xenon as expected, with various trace impurities also present in the background environment. The scan was taken with I_{ck} set at 1.0 A and $I_h = 1.5$ A. Because the QMS ionizes neutrals but its electron energy was set to just 25 eV, ions and neutrals from the cathode and the chamber background both contribute to the spectrum of Fig. 1. Although the scan started at $m/e = 1$, the signal there is dominated, due to finite resolution, by the intrinsic characteristic that all ions are transmitted at $m/e = 0$. A peak corresponding to $m/e = 138$, the most abundant isotope of singly ionized barium, is apparent in Fig. 1. Except at a very high cathode temperature, barium could not be observed. The largest peak was obtained after cathode ignition, before reducing I_h. Ba was also observable under the conditions $V_{ck} = 0$, $I_{ck} = 0$, and $I_h \geq 2.3$ A. BaO was not detected. Barium detection would be enhanced by running the ionizing filament at lower energy than the 25-eV limit of this instrument, with high detector gain.

Presented as Paper 99-0454 at the AIAA 37th Aerospace Sciences Meeting, Reno, NV, 11–14 January 1999; received 12 April 1999; revision received 26 May 1999; accepted for publication 15 July 1999.

*Research Scientist, M5-754, P.O. Box 92957, Technology Operations, Mechanics and Propulsion Department, Los Angeles, CA 90009-2957. Member AIAA.